


Under-ice mid-frequency acoustic transmission and communication in two Arctic Ocean environments

Dag Tollefsen,^{a)}  Paul van Walree, Trond Jenserud, and Vidar Forsmo

Norwegian Defence Research Establishment (FFI), Box 115, 3191 Horten, Norway

dag.tollefsen@ffi.no, Paul.vanWalree@ffi.no, Trond.Jenserud@ffi.no, Vidar.Forsmo@ffi.no

Abstract: This paper presents data from mid-frequency (4–8 kHz) under-ice acoustic transmission and communication experiments in the Nansen Basin and in the Beaufort Sea of the Arctic Ocean. Measured impulse responses to range ~ 10 km showed considerable delay spread between distinct groups of arrivals due to surface-ducted and bottom-reflected paths. The relative strengths of these groups depend on duct and under-ice properties. We demonstrate that despite shallow (~ 25 m) source/receiver depths, good communication performance can be achieved in both environments when exploiting the bottom-reflected arrivals. Simulations with the Bellhop ray model support the findings. © 2023 Author(s). All article content, except where otherwise noted, is licensed under a Creative Commons Attribution (CC BY) license (<http://creativecommons.org/licenses/by/4.0/>).

[Editor: Charles C. Church]

<https://doi.org/10.1121/10.0017325>

Received: 2 September 2022 **Accepted:** 26 January 2023 **Published Online:** 22 February 2023

1. Introduction

The thinning of and decrease in sea ice in the Arctic and changes in oceanographic conditions affect sound propagation and, hence, performance of under-ice communication and navigation systems.¹ Specifically, in the Pacific sector of the Arctic Ocean, seasonal inflow of warm water (Pacific Summer Water) creates an upper (surface) duct and a lower (subsurface) sound-speed duct. The lower duct, the Beaufort Duct (depth ~ 60 – 200 m), can provide favorable conditions for long-range propagation,^{2–4} and can be exploited for communication and navigation purposes.^{5,6} In the Atlantic sector of the Arctic Ocean, inflow of warm Atlantic Water⁷ can potentially affect propagation conditions in a similar manner, although this has yet to be observed. Under-ice experiments in the Fram Strait have shown impulse responses consistent with classical upward-refracting Arctic conditions⁸ and that a surface duct in the Fram Strait (depth to ~ 200 m) can yield favorable long-range communication performance despite ice cover.⁹

In cases where the advantage of a subsurface sound-speed duct cannot be exploited, either due to permanent or seasonal oceanographic conditions or due to acoustic system depth limitations, it is of interest to probe transmission in the surface ducts bounded above by an ice cover. To this end, this paper presents results from two recent mid-frequency (4–8 kHz) acoustic experiments in the Nansen Basin (NB) and the Beaufort Sea (BS), respectively, with sources and receivers at shallow depths of ~ 25 m. Signals are processed for wideband delay profiles,¹⁰ with arrival structures interpreted by use of the Bellhop¹¹ ray model. Results from acoustic communication experiments demonstrate that bottom-interacting paths can enable good communication performance despite challenging duct conditions.

2. Data and processing

2.1 Experiments and areas

An under-ice ($\sim 80\%$ cover of first-year ice) acoustic experiment was conducted by the Norwegian Defence Research Establishment (FFI) in August 2019 in the NB during a research cruise with the Royal Norwegian Coast Guard icebreaker RNCGV Svalbard¹² [see Fig. 1(a) for location and Fig. 1(b) for a photo]. Two receive hydrophones [Brüel & Kjaer (Nærum, Denmark) models 8104 and 8106] were suspended from a drifting ice floe, located at approximately 83.6° N and 026.1° E at the time of deployment. An omnidirectional acoustic source (Neptune Sonar Ltd. T-170) was deployed from the ship stern, with transmit (Tx) stations at approximate ranges of 10, 20, and 40 km from the receiver (Rx) station. The Tx stations were located within pools (extent ~ 0.5 km) of open water. The source, at preset nominal depths of 20 and 90 m, transmitted 4–8 kHz signals at a source level (SL) of 185 dB re $1 \mu\text{Pa}^2 \text{m}^2$. The signal sequence consisted of a variety of channel probe signals and communication packets.¹³ Analyzed here is a 250-ms linear frequency modulated (LFM)

^{a)} Author to whom correspondence should be addressed.

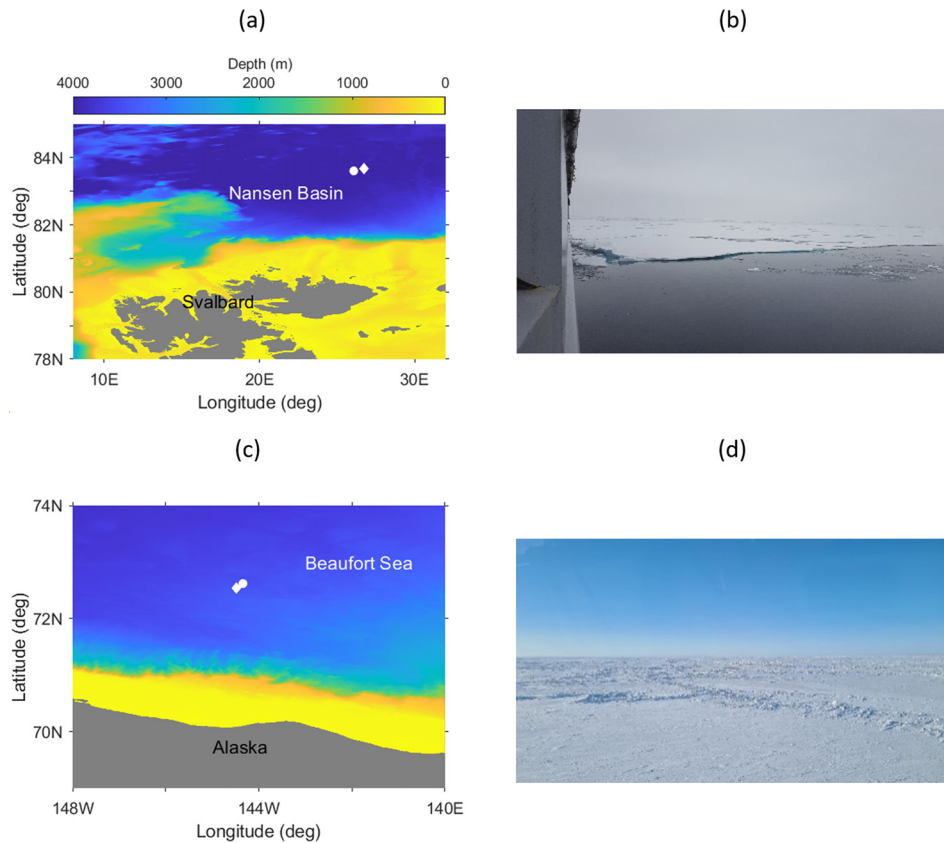


Fig. 1. (a) Site of NB experiment. Symbols indicate Tx (diamond) and Rx (circle) positions. Color code is water depth in m. (b) Photo of ice conditions from the NB experiment. (c) Site of and (d) photo of ice conditions from the BS experiment.

chirp signal with a bandwidth of 4 kHz at a center frequency of 6 kHz, repeated eight times at a repetition rate of 4 s. The data processing is described in Ref. 10. A depth-tilt sensor [Star-Oddi (Gardabaer, Iceland) DST] monitored the source depth. Global Positioning System (GPS) recorders were mounted on the Rx station and on the ship stern.

A second experiment was conducted by FFI in the BS on March 17, 2022, during the Ice Exercise 2022 hosted by the U.S. Navy's Arctic Submarine Laboratory [see Fig. 1(c) for location and Fig. 1(d) for a photo]. A full (~99%) cover of multi-year ice with ridges described ice conditions. The experiment used the equipment described above; however, due to logistics considerations, the transmitter was at a fixed site (73.2° N and 144.3° W), with the portable Rx station set up (via helicopter transport) at nominal ranges of 2, 5, and 11 km. To reduce potential risk of hydrophone cable freezing during retrieval, the Rx hydrophones were limited to depths preset to 10 and 25 m, while Tx depths were maintained at 20 and 90 m. For this experiment, a 4–8 kHz LFM probe signal was transmitted at a SL of 190 dB re 1 $\mu\text{Pa}^2 \text{m}^2$.

Table 1 summarizes parameters and ice conditions for the two experiments.

Table 1. Experiment parameters.

Quantity	Unit	NB	BS
Position		83.6° N 023.1° E	72.3° N 144.3° W
Date		August 30, 2019	March 17, 2022
Water depth average	m	4003	3436
Source depths	m	20, 90	20, 90
Receiver depths	m	25, 90	10, 25
Range	km	10.64	11.74
Ice fraction		0.78	0.99
Ice thickness	m	1.20	1.86

2.2 Environmental data

Bathymetric data were retrieved from the International Bathymetric Chart of the Arctic Ocean (IBCAOV4.1).¹⁴ Daily mean fields for ocean model temperature (T) and salinity (S) and ice-cover parameters were retrieved from the Copernicus Marine Environment Monitoring Service (CMEMS).¹⁵

In the NB, T profiles were also measured from the ship using expendable bathythermograph (XBT) casts (to depth 760 m) at the Rx and Tx stations. Figure 2(a) shows an XBT profile from the T10 (Tx at range ~10 km) station. Each measured profile was merged in depth with the closest CMEMS profile using spline interpolation.¹² Sound speed profiles (SSPs) were then computed using the Chen and Millero equation.¹⁶ Figure 2(b) shows the resulting SSP (to depth 360 m) at T10. The surface duct to ~200 m depth is due to an upper layer of cold water. The increase in T from approximately -1.7°C to -0.3°C over the upper 2 m is presumed due to surface heating in the open-water pool at the location. Beneath the surface duct, there is near constant sound speed to 1000 m; sound speed then increases to 1512 m/s at the seabed (depth 4003 m).

For the BS experiment, T and S profiles were measured at the Tx position using a handheld SD204 instrument (SAIV Instruments) to depth 365 m. Figures 2(a) and 2(b) show the measured T profile and the computed SSP. The surface duct to ~50 m depth is due to cold water masses (T -1.5°C), bounded below by warmer water with a maximum of +0.6°C at 48 m depth. Beneath, T decreases to a minimum of -1.44°C at 190 m depth and then increases to a maximum of 1503 m/s at the seabed (depth 3436 m). The warm water creates the *double duct* condition.¹⁻⁴ Ice conditions were measured through drill holes (2.1 and 1.5 m, respectively, at the Tx and R10 stations).

2.3 Wideband delay profiles

A linear time-varying channel model is adopted where the received signal is given by the convolution of the transmitted signal with the time-varying impulse response $h(t, \tau)$. Impulse responses are calibrated for the propagation loss by defining the transmitted signal, $x(t)$, as the product of range and acoustic pressure in the far field of the source and the received signal, $y(t)$, as the pressure at the Rx. A correlative channel sounder is applied to recorded probe signals, yielding a band limited impulse response estimate $\tilde{h}(t, \tau)$. The delay profile is given by¹⁰

$$\tilde{P}(\tau) = B^{-1} \mathbb{E} \left[\left| \tilde{h}(t, \tau) \right|^2 \right], \tag{1}$$

where B is the bandwidth. This profile has units of $\text{m}^{-2} \text{s}^{-1}$ and satisfies the relationship

$$\mathbb{E} \left[|y(t)|^2 \right] = \mathbb{E} \left[|x(t)|^2 \right] \int_0^\infty \tilde{P}(\tau) d\tau. \tag{2}$$

The delay profile is converted to a sound pressure level (SPL) profile through

$$P_{SPL}(\tau) = 10 \log_{10} \tilde{P}(\tau) - 10 \log_{10} B + SL, \tag{3}$$

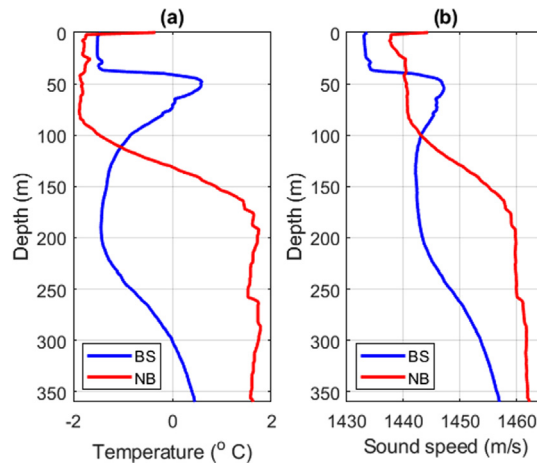


Fig. 2. (a) Measured T profiles and (b) computed SSPs versus depth to 360 m for the NB (red) and BS (blue) experiments.

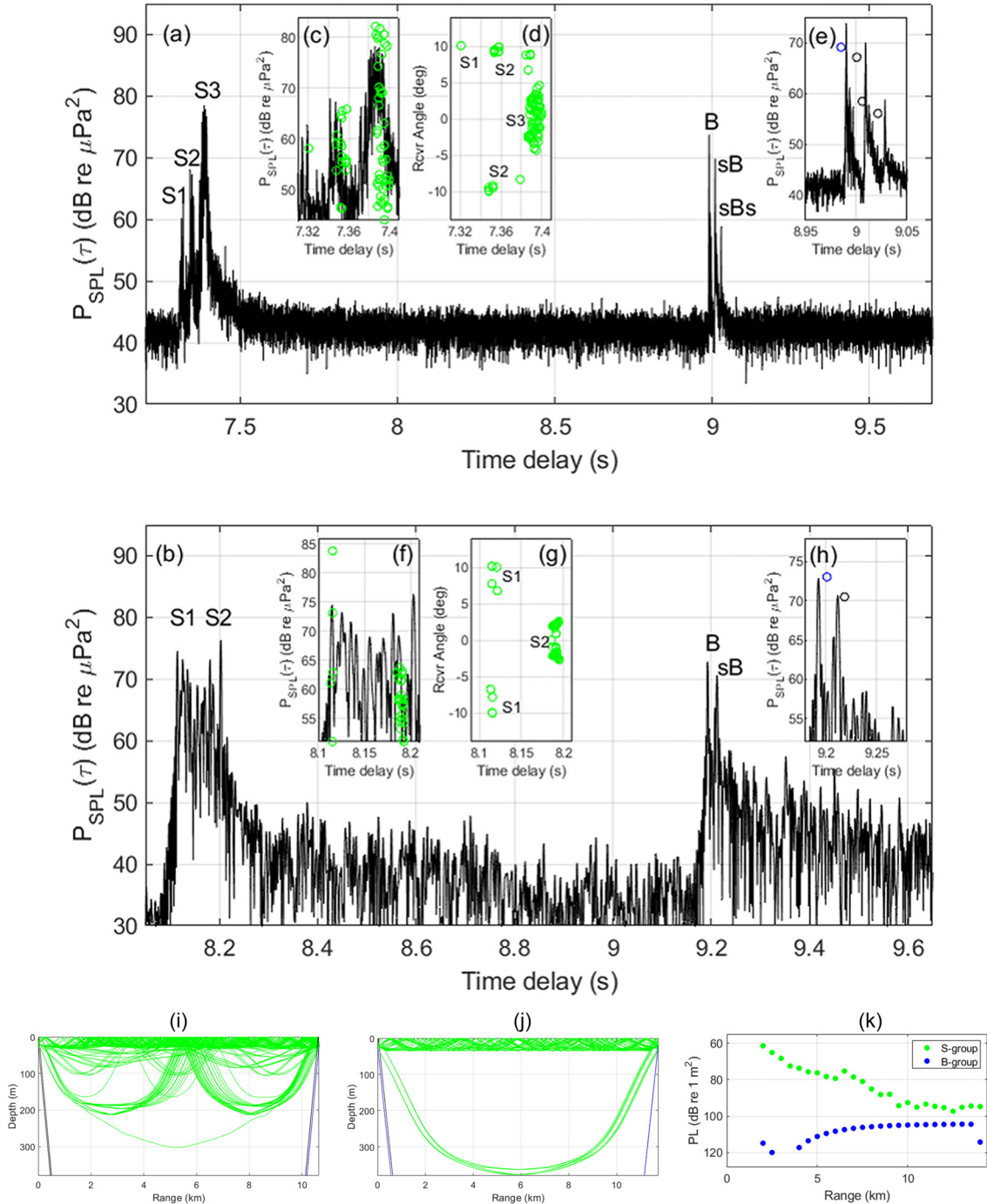


Fig. 3. (a) and (b) Measured delay profiles at range ~ 10 km, for NB and BS experiments, respectively. (c) and (f) Measured delay profiles and modeled ray arrivals (circles) for S-group arrivals. (d) and (g) Modeled ray arrival angles vs arrival time for S-group arrivals. (e) and (h) Measured delay profiles and modeled ray arrivals (circles) for B-group arrivals. (i) and (j) Eigenray plots for the NB and BS environments (to depth 380 m), respectively. (k) Modeled propagation loss for S- and B- group arrivals in the BS environment for ranges 2–14 km. All plots for Tx/Rx depths 20 m/25 m.

with SL the source level in dB re $1 \mu\text{Pa}^2 \text{m}^2$. The peak value of each multipath arrival in this profile gives the received mean square SPL due to that arrival. Modeled delay profiles (peak values) can be obtained by

$$P_M(\tau_j) = 20 \log_{10} A_j + SL, \quad (4)$$

where (τ_j, A_j) is the arrival time and amplitude, respectively, of the j th ray modeled at the band center frequency for a unit strength point source.

3. Results

3.1 Measured delay profiles

Figures 3(a) and 3(b) show measured delay profiles from transmissions at nominal ranges of 10 km at Tx/Rx depths 20 m/25 m, from the NB and BS experiments, respectively.

For the NB, Fig. 3(a), the delay profile consists of a group of surface-ducted (S) arrivals, and a later-arriving group of bottom-reflected (B) arrivals. The delay spread is ~ 1.6 s between the groups. The S-group can be separated into three, S1–S3, with a reverberant tail thereafter. S3 is the strongest, ~ 6 dB stronger than the B-group. The B-group consists of three distinct arrivals, B, sB, and sBs, in order of time delay, s indicating a surface reflection (further discussed in Sec. 3.2).

For the BS [Fig. 3(b)], the delay spread between the S- and B-groups of arrivals is ~ 1.1 s. The S-group can be separated into S1 and S2, with ~ 0.1 s internal delay spread. S2 is here ~ 3 dB stronger than the B-group arrivals.

Further insight into the delay profile structure is gained through numerical modeling (Sec. 3.2).

3.2 Modeled delay profiles

We used the Bellhop coherent raytrace model¹¹ to model delay profile peak arrivals. Environment input was a SSP (Sec. 2.2), a sloping seabed, and a range-dependent ice-cover model via reflection coefficients. Scattering loss due to under-ice roughness was modeled using the Kirchhoff approximation, assuming a spectrum described by the gamma distribution. The coherent reflection coefficient is $R_{TOT} = R(\theta, f) \cdot R_C(\mu, \sigma) \cdot R_S$, where the terms represent the frequency f and grazing angle θ dependent local reflection coefficient for an elastic ice model, scattering loss for mean ice thickness μ and roughness standard deviation σ , and a shadowing correction,¹⁷ respectively. This model is a simplification over actual sea-ice properties but accounts for the principal loss contribution due to roughness at the frequencies and long-range propagation situations considered here.^{2,9} For sea-ice acoustic parameters, we used p - and s -wave speeds of 3100 and 1800 m/s, respectively, a density of 0.91 g/cm^3 , and wave attenuations of 0.22 and $0.65 \text{ dB}/\lambda$. For NB, the surface model used open water near Tx, followed by ice with $\mu = 1.20 \text{ m}$, $\sigma = 0.18 \text{ m}$, with smooth ice ($\sigma = 0.03 \text{ m}$) near Rx. For BS, we used smooth ice near Tx, followed by rough ice with $\mu = 1.85 \text{ m}$, $\sigma = 0.30 \text{ m}$. The seabed was modeled as an acoustic half space with sound speed 1559 m/s, density 1.35 g/cm^3 , and attenuation $0.10 \text{ dB}/\lambda$.¹²

Model peak arrivals are plotted with colored symbols in insets (c)–(e) and (f)–(h) of Fig. 3, respectively, for the NB and BS experiments.

For the NB [Fig. 3(c)], the model captures an S1-arrival and groups of S2- and S3-arrivals (all S-arrivals in green). The decaying tail observed after the S-arrivals, due to diffuse under-ice scatter, is not captured with the type of ice-reflection model used here. Figure 3(d) shows ray angles vs arrival time for all S-arrivals. S1 and S2 are due to steeper-angle rays ($\sim 9^\circ$ – 10° grazing angle), while S3-arrivals are due to shallow-angle rays. Figure 3(e) shows that the B-arrival (blue) and subsequent arrivals of the B-group (black), and their relative time differences, are modeled well. The presence of near equal levels of B- and sB-arrivals is consistent with a source in open water (i.e., low loss at the surface reflection

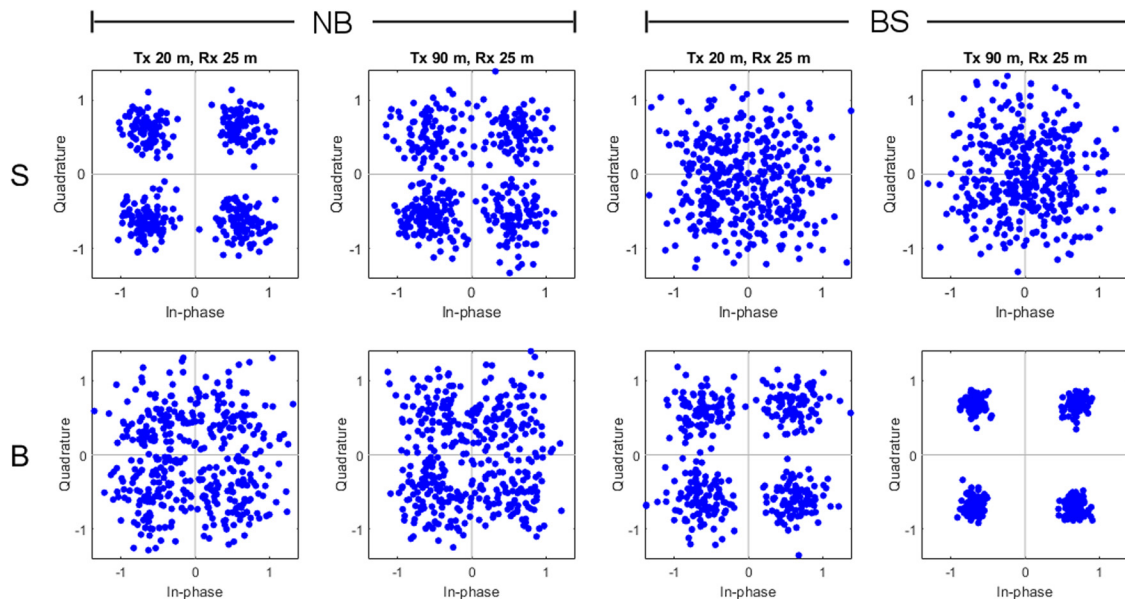


Fig. 4. Received symbol constellations for the S- and B-group arrivals, for the NB and BS experiments. Each dot represents two bits.

Table 2. Communication results for a 256-bit FRSS packet over a horizontal range of ~ 10 km. Bit errors are measured after the Viterbi decoder.

Experiment	Tx/Rx depth (m)	Group	Input SNR (dB)	Output SNR (dB)	Bit errors
NB	20/25	S	20.0	10.7	0
		B	8.6	3.9	0
NB	90/25	S	19.1	7.4	0
		B	8.2	5.0	0
BS	20/25	S	15.8	0.2	28
		B	10.7	8.7	0
BS	90/25	S	15.4	0.7	72
		B	19.0	16.9	0

near the source). The ~ 14 dB lower levels of the Bs- and sBs-arrivals (with respect to B) are due to under-ice scattering loss near Rx. (Bs is coincident with sB and not discernible in data.) The model/data discrepancy for the B-arrival suggests an error in the seabed model.

For the BS [Fig. 3(f)], the model captures groups of S1- and S2-arrivals. Figure 3(g) shows that S1-arrivals are due to steeper-angle rays ($\sim 6^\circ - 10^\circ$ grazing angle), while S2-arrivals are due to shallow-angle rays. The delay spread and relative levels of S1 and S2 are well modeled. Figure 3(h) shows that the B- and sB-arrivals are accurately modeled, while further arrivals are weak due to high under-ice loss near Rx and are not readily discernible in data.

Figures 3(i) and 3(j) show eigenray plots for the NB and BS experiments, respectively. Figure 3(i) shows that for the NB, steeper-angle rays (S1 and S2) transit the surface duct (turning depths ~ 300 m and ~ 210 m, respectively), while shallow-angle rays (S3) reside in the upper part of the surface duct. For the BS, Fig. 3(j) shows that steep-angle rays (S1) transit into the Beaufort duct (turning depths ~ 370 m), while shallow-angle rays (S2) reside in the upper duct.

A notable feature in the BS environment is the strength of the B-type relative to S-type arrivals; this depends on source-Rx range. Figure 3(k) shows modeled propagation loss for S- and B-group arrivals, separately, at ranges of 2–14 km, in the BS model environment. The relative level of B-group arrivals increases with source-Rx range.

3.3 Acoustic communication

In both experiments, various communication packets were transmitted. Doppler spread was small in NB and mainly due to drifting of the transmitter ship and the Rx ice floe. Doppler spread was vanishingly small in BS, resulting in a static channel on the signaling time scale. The challenge in these environments is the large delay spread. A defining characteristic of both NB and BS is that communication packets arrive twice, once via the S paths and once via the B paths. Demodulation results for NB revealed that decoding was fairly successful at a range of 10 km, although some packets were lost due to collisions between S- and B-arrivals.¹³

To avoid collisions between different packets in BS, the spacing between successive packets was increased in the Tx schedule. However, this does not prevent a packet from colliding with itself if its length exceeds the travel time difference between S and B. Communication with long packets requires robustness measures to deal with the interference of the bottom reflection. A simpler approach is to use short packets. This is illustrated for the frequency-repetition spread spectrum (FRSS) modulation, considering a packet with 256 information bits and three subbands.¹⁰ The packet duration is 0.86 s. Feeding the recorded BS hydrophone data to the standard modem Rx results in two detections and two decoding results for each transmitted packet.

Figure 4 shows the equalized symbol constellations, and Table 2 summarizes performance metrics, for a typical experiment Tx cycle. The output signal-to-noise ratio (SNR)¹⁰ is a measure of the communication quality, where a high value corresponds to compact clouds and a low probability of bit error. For comparison, the figure and table include NB results for the same configurations. Unlike the BS results, these were not obtained for the raw hydrophone data, which contain colliding packets, but for realistic channel replay with the measured $\hat{h}(t, \tau)$.

In all cases, the Rx detects and demodulates the S- and B-groups separately. It is applied with the standard modem settings, which include an equalizer length of 24 ms.¹⁰ Reference 10 quantitatively shows that (in the absence of Doppler effects) all multipath arrivals within the equalizer span contribute useful acoustic power, whereas the remaining paths give rise to intersymbol interference (ISI). This can explain why the poorest modem performance is observed for the S-group in BS. The delay spread of the received packet is ~ 100 ms, and a large part of the received signal power is ISI. By contrast, the equalizer has access to the power of the two strongest arrivals for the packet received via the BS bottom, and the ISI paths are weak. This yields a good modem performance. The situation is reversed for the NB, where the S packet has a better useful signal-to-ISI ratio than the B-group.

Communication with long packets results in a collision between the S- and B-groups, which can be mitigated by reducing the data rate.¹³ Sparse channel equalization techniques have potential in these environments, although automated algorithms may be challenged by the long delay of the B-group.

4. Summary

This paper examined mid-frequency (4–8 kHz) acoustic under-ice transmission in two distinct deep-water environments in the Arctic Ocean: under partial (~80%) cover of first-year ice in late summer conditions in the NB and full (~99%) cover of multi-year ice and winter/spring conditions in the BS. The acoustic experiments used shallow source/receiver combinations to probe transmission channel characteristics and assess upper-duct acoustic communication performance. Measured impulse responses to range ~10 km showed considerable delay spread due to two distinct groups of arrivals: surface-ducted and delayed bottom-reflected arrivals. The relative levels between peak arrivals in these groups varied between experiments: Peak B-group arrivals were ~6 dB lower in the NB experiment and ~3 dB lower in the BS experiment. Bellhop was used to model measured delay profile peak arrivals. Time spreads were modeled to good accuracy, but amplitudes could not be modeled to high accuracy due to simplifications in the ice-scatter model and insufficient knowledge of *in situ* under-ice and seabed properties. The significance of bottom-reflected arrivals for acoustic modem performance was demonstrated. For long modem signals, they interfere with the surface-ducted arrivals, but for short signals, the two arrival groups are decoded separately by the modem, revealing improved modem performance for the bottom-reflected sound in the BS.

Acknowledgments

The authors thank the crew of the RNCGV Svalbard Svalbard and the staff of the U.S. Navy's Arctic Submarine Laboratory for logistics support and assistance with the experiments.

References and links

- ¹P. F. Worcester, M. A. Dzieciuch, and H. Sagen, "Ocean acoustics in the rapidly changing Arctic," *Acoust. Today* **16**, 55–64 (2020).
- ²M. Ballard, M. Badiey, J. D. Sagers, J. A. Colosi, A. Turgut, S. Pecknold, Y.-T. Lin, A. Proshutinsky, R. Krishfield, P. F. Worcester, and M. A. Dzieciuch, "Temporal and spatial dependence of a yearlong record of sound propagation from the Canada Basin to the Chukchi Shelf," *J. Acoust. Soc. Am.* **148**, 1663–1680 (2020).
- ³T. F. Duda, G. Zhang, and Y.-T. Lin, "Effects of Pacific Summer Water layer variations and ice cover on Beaufort Sea underwater sound ducting," *J. Acoust. Soc. Am.* **149**, 2117–2136 (2021).
- ⁴A. B. Baggeroer and J. M. Collis, "Transmission loss for the Beaufort Lens and the critical frequency for mode propagation during ICES-18," *J. Acoust. Soc. Am.* **151**, 2760–2772 (2022).
- ⁵L. Freitag, K. Ball, J. Partan, P. Koski, and S. Singh, "Long range acoustic communications and navigation in the Arctic," in *Proceedings of OCEANS 2015—MTS/IEEE Washington*, Washington, DC (October 19–22, 2015).
- ⁶E. C. Bhatt, O. Viquez, and H. Schmidt, "Under-ice acoustic navigation using real-time model-aided range estimation," *J. Acoust. Soc. Am.* **151**, 2656–2671 (2022).
- ⁷I. V. Polyakov, A. V. Pnyushkov, M. B. Alkire, I. M. Ashik, T. M. Baumann, E. C. Carmack, I. Goszczko, J. Guthrie, V. V. Ivanov, T. Kanzow, R. Krishfield, R. Kwok, A. Sundfjord, J. Morison, R. Rember, and A. Yulin, "Greater role for Atlantic inflows on sea ice loss in the Eurasian Basin of the Arctic Ocean," *Science* **356**, 285–291 (2017).
- ⁸G. Hope, H. Sagen, E. Storheim, H. Hobæk, and L. Freitag, "Measured and modeled acoustic propagation underneath the rough Arctic sea-ice," *J. Acoust. Soc. Am.* **142**, 1619–1633 (2017).
- ⁹L. Freitag, P. Koski, A. Morozov, S. Singh, and J. Partan, "Acoustic communications and navigation under Arctic ice," in *Proceedings of 2012 Oceans*, Hampton Roads, VA (October 14–19, 2012).
- ¹⁰P. A. van Walree and M. E. G. D. Colin, "In situ performance prediction of a coherent acoustic modem in a reverberant environment," *IEEE J. Ocean. Eng.* **47**(1), 236–254 (2022).
- ¹¹M. B. Porter, "The BELLHOP manual and user's guide (preliminary draft)," Technical Report (HLS Research Inc., La Jolla, CA, 2011).
- ¹²D. Tollefsen, P. A. van Walree, T. Jensrud, and V. Forsmo, "Mid-frequency under-ice acoustic transmission in the Nansen Basin," in *Proceedings of Oceans 2021: San Diego–Porto*, San Diego, CA (September 20–23, 2021).
- ¹³P. A. van Walree, D. Tollefsen, and V. Forsmo, "Under-ice acoustic communication in the Nansen Basin," in *Proceedings of the 2021 Fifth Underwater Communications and Networking Conference (UComms)*, Lercis, Italy (August 31–September 2, 2021).
- ¹⁴International Bathymetric Chart of the Arctic Ocean (IBCAO), https://www.gebco.net/about_us/committees_and_groups/scrumbcao/ibcao_v4_1.html (Last viewed August 22, 2022).
- ¹⁵Copernicus Marine Environment Monitoring Service, "Arctic Ocean physics analysis and forecast," <https://doi.org/10.48670/moi-00001> (Last viewed January 19, 2023).
- ¹⁶Oceanography Toolbox, available at <https://sea-mat.github.io/sea-mat/#sea-mat-matlab-tools-for-oceanographic-analysis> (Last viewed January 19, 2023).
- ¹⁷J. Ogilvy, *Theory of Wave Scattering from Random Rough Surfaces* (Taylor & Francis, London, 1991).